





BALTICA Volume 38 Number 2 December 2025: 143-159

https://doi.org/10.5200/baltica.2025.2.3

Post-magmatic alteration in the Kabeliai granite, Lithuania: evidence from petrography, mineral chemistry, and accessory minerals

Olga Demina*, Gražina Skridlaitė, Laurynas Šiliauskas, Marcin Łącki, Beata Marciniak-Maliszewska, Bogusław Bagiński

Demina, O., Skridlaitė, G., Šiliauskas, L., Łącki, M., Marciniak-Maliszewska, B., Bagiński, B. 2025. Post-magmatic alteration in the Kabeliai granite, Lithuania: evidence from petrography, mineral chemistry, and accessory minerals. *Baltica* 38 (2), 143–159. Vilnius. ISSN 0067-3064.

Manuscript submitted 1 September 2025 / Accepted 29 October 2025 / Available online 20 November 2025

© Baltica 2025

Abstract. This study reconstructs the sequence of secondary mineral transformations in the Kabeliai granite (southern Lithuania) based on detailed petrographic, mineral chemical, and isotopic data from samples obtained from a drill core Marcinkonys-7. The selected samples represent various lithologies and grades of alteration, from melanocratic diorite to pegmatitic granite. Several alteration steps were identified. The earliest is marked by the late-magmatic re-equilibration of feldspars and accessory minerals. The following subsolidus re-equilibration leads to perthitic textures and albite replacement. The later stage reflects infiltration of Na–Ba–SO₄-bearing fluids, which caused feldspar metasomatism, biotite alteration, barite precipitation, and partial titanite breakdown. Finally, F–CO₂-rich fluids induced advanced replacement of titanite by anatase, calcite, and REE-carbonates, accompanied by widespread albitisation, hematite formation, and REE mobilisation. The observed mineral assemblages and textural relationships are consistent with progressive fluid-driven modification under increasing fO₂ and decreasing temperature. These results demonstrate that accessory minerals such as titanite and apatite can preserve complex records of post-magmatic processes and highlight the role of oxidising REE-bearing fluids in the late evolution of granitic systems.

Keywords: granite alteration; titanite replacement; fluid-rock interaction; REE mobilisation; albitisation; metasomatism; Mesoproterozoic; secondary mineralisation

Olga Demina* (olga.demina@gamtc.lt, b https://orcid.org/0000-0001-8239-2367),

Gražina Skridlaitė (grazina.skridlaite@gamtc.lt), Laurynas Šiliauskas (laurynas.siliauskas@gamtc.lt),

State Scientific Research Institute Nature Research Centre, Akademijos 2, LT-08412, Vilnius, Lithuania;

Marcin Łącki (m.lacki2@uw.edu.pl), Beata Marciniak-Maliszewska (b.maliszewska@uw.edu.pl), Laboratory of Electron Microscopy, Microanalysis and X-Ray Diffraction, Faculty of Geology, University of Warsaw,

Bogusław Bagiński (b.baginski l@uw.edu.pl),

Department of Geochemistry, Mineralogy, and Petrology, Faculty of Geology, University of Warsaw, ul. Zwirki i Wigury 93, PL-02-089 Warszawa, Poland

*Corresponding author

INTRODUCTION

Granitoid rocks are produced in almost all tectonic settings and are considered reasonably chemically stable and resistant to secondary alteration. However, an increasing number of studies show that even apparently fresh granites can undergo complex, multi-stage post-magmatic transformations that significantly modify their mineralogical and geochemi-

cal characteristics. For example, high Ba content in K-feldspar suggests incipient fluid involvement (Vernon 2004; Shelley 1993). Morad *et al.* (2009) report that the replacement of primary titanite by anatase, calcite, and REE-bearing minerals is consistent with a fluid-mediated breakdown process under oxidising, F-CO₂-rich conditions (Feng *et al.* 2023). Therefore, understanding such transformations is essential for reconstructing magmatic-hydrothermal evolution and

for assessing the remobilisation of critical elements such as rare earth elements (REE), U, Th, etc.

The Kabeliai granite in southern Lithuania offers a valuable case for investigating fluid-assisted post-magmatic processes. The selected Marcinkonys-7 drill core intersects multiple intrusive phases and alteration zones within the plutonic body and its contact with weakly foliated melanocratic diorite. This enables direct comparison between relatively unaltered mafic rocks and metasomatically modified felsic domains. The vertical continuity of the core provides a unique opportunity to investigate both primary magmatic features and superimposed metasomatic overprints, capturing transitions from relatively unaltered to strongly modified domains within a single coherent section.

This work aims to reconstruct the sequence of secondary mineralogical processes affecting the Kabeliai granite by integrating petrographic observations and mineral chemical data. Raman spectroscopy was additionally employed to distinguish polymorphs such as rutile and anatase and to verify fine-grained mineral intergrowths and alteration products. The results offer new insights into fluid-rock interaction pathways, element mobility, and the post-crystallisation evolution of evolved granitic systems.

GEOLOGICAL SETTING

The studied Mesoproterozoic Marcinkonys granitoid massif crosscuts two major structures in the crystalline basement of south-eastern Lithuania: the 1.89 Ga East Lithuanian belt (part of the Latvian-East Lithuanian domain; Bogdanova et al. 2015) and 1.84–1.87 Ga SE Mid-Lithuanian domain (SE MLD; Fig. 1A; Skridlaite et al. 2021). In the vicinity of the Marcinkonys massif, the East Lithuanian belt is composed mainly of metamorphosed granite-granodiorite-diorite rocks (mostly orthogneisses) with bodies of metamorphosed gabbro (Fig. 1A). To the north, several iron ore bodies are hosted by metasedimentary dolomites and skarns (Skridlaite et al. 2019). The iron ore bodies are steeply plunging toward NE and are overlayed by metavolcanics of felsic composition (Skridlaite et al. 2021). The SE MLD rocks are slightly metamorphosed granodiorites and diorites of Volcanic Island Arc (VIA) affinity (Fig. 1A).

The Marcinkonys granitoid massif exhibits a wide range of lithologies, including melanocratic diorites, leucocratic granites, and pegmatitic facies, reflecting multiple intrusive pulses and a complex magmatic evolution. Because the Marcinkonys-4 and Marcinkonys-7 drillings lie near the village of

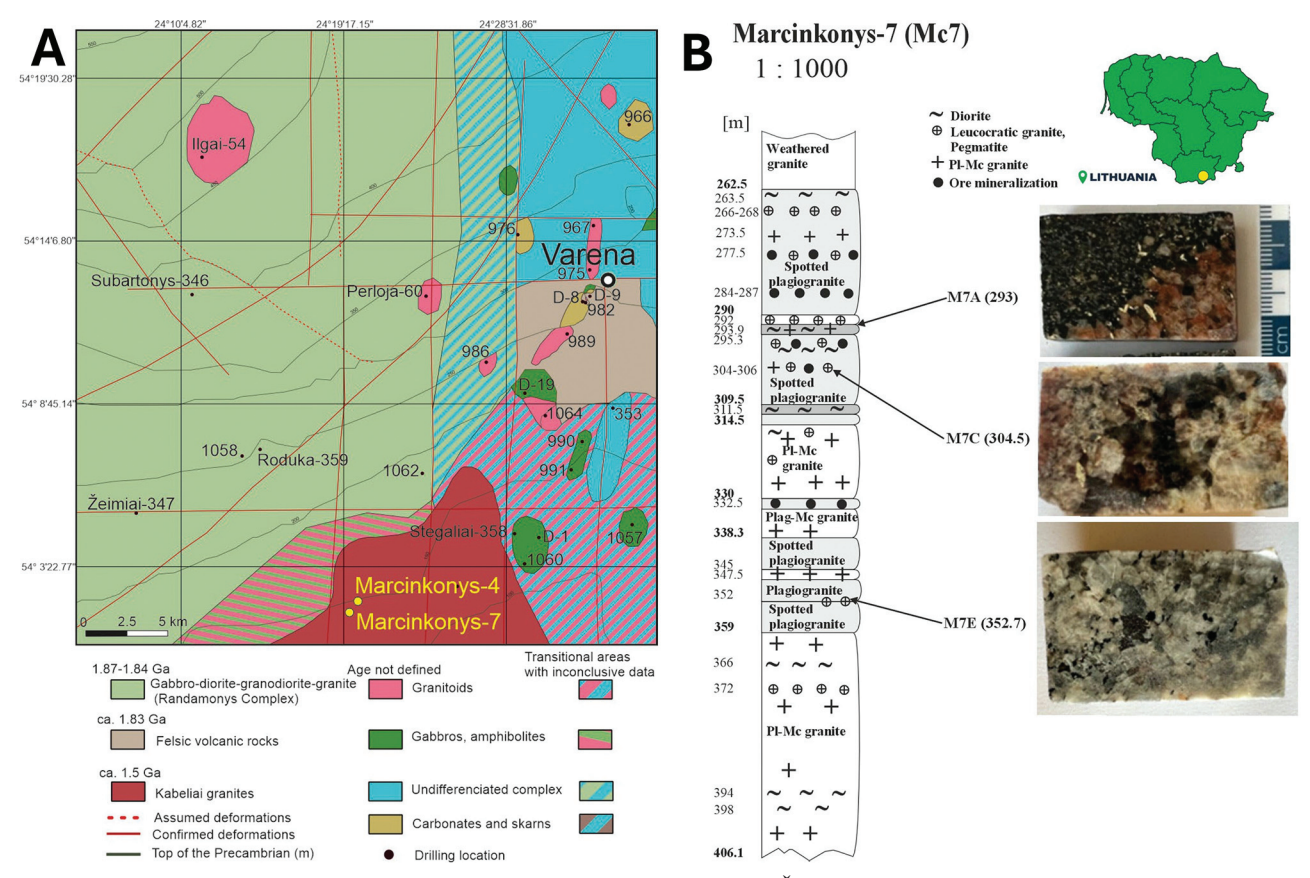


Fig. 1 Sketch map of the crystalline basement of southern Lithuania (by Šiliauskas, from Skridlaite *et al.* 2024) with location of the Marcinkonys-7 drill site (A). Cross-section of the Marcinkonys-7 borehole with the studied rock samples and outline map of Lithuania with marked borehole location (licensed under free license from vecteezy.com) (B)

Kabeliai (SE Lithuania), the name "Kabeliai granites" is used in some cases to refer to all granitoids of the Marcinkonys massif. U-Pb zircon dating from Marcinkonys-4 yields 1505 ± 11 Ma (Sundblad *et al.*) 1994). Marcinkonys-4 is located $\approx 1 \text{ km}$ (940 m) from the Marcinkonys-7 borehole studied in this paper. In addition, Re-Os dating of molybdenite from mineralised zones within the same intrusion produced an age of 1486 ± 5 Ma (Stein et al. 1998), interpreted as the timing of hydrothermal ore mineralisation. These ages bracket the magmatic and early post-magmatic history of the pluton and provide a temporal framework for interpreting secondary alteration features observed in the present study. Considering the rock compositions and age, the granitoids might be an eastward extension of the 1.53–1.50 Ga Mazury Anorthosite-Mangerite-Charnockite-Granite (AMCG) suite (cf. Skridlaite et al. 2008; Wiszniewska et al. 2002; Vejelyte et al. 2015).

The Marcinkonys-7 drilling intersects several intrusive phases, alteration zones, and accumulations of ore minerals (Fig. 1B); therefore, it was chosen for further investigations. Beneath the weathering crust, from 262.5 m, a medium-grained, spotted (with mafic enclaves) plagiogranite continues down to 314.5 m including minor intervals of diorite (e.g. 293–293.9; 309.5–311.5 m), leucocratic, pegmatitic (268, 277.5, 292-293, 295.3, 304-306 m) and equigranular plagiogranite-microcline granite (Pl-Mc granite 273.5, 304, Fig. 1B). The red-coloured Pl-Mc granite with rare inclusions of pegmatite, diorite and sulphideand Fe-Ti oxide-bearing plagiogranite (330–332.5 m) continues down to 338.3 m. The lower interval is composed of leucocratic and spotted (enclave-rich) plagiogranite with lenses of biotite and Pl-Mc granite. The lowest part of the cross-section, from 359 to 406.1 m, is made of equigranular and porphyritic Pl-Mc granite with thin layers of diorite and pegmatite (Fig. 1B).

Three samples were selected for a detailed investigation: M7A, M7C, and M7E. These samples represent different lithologies and degrees of alteration within the Kabeliai granite body, ranging from melanocratic diorite (M7A) to leucocratic granites (M7C and M7E), including pegmatitic domains. The selected rocks are coarse- to very coarse-grained, which is essential for tracking alteration processes that operate primarily along fractures and grain boundaries. Their mineralogical composition, dominated by quartz, K-feldspar, and plagioclase, makes them relatively resistant to complete alteration, thus preserving unaltered cores alongside altered rims. This allows direct observation of both primary magmatic assemblages and secondary alteration products within the same thin section, providing a robust framework for reconstructing fluid-rock interaction pathways.

METHODS

Petrographic analysis was conducted using a polarising microscope Nikon Eclipse LV100N POL with an epi-illumination attachment at the Nature Research Centre, Lithuania, to investigate mineral textures, microstructures, and alteration patterns.

Whole-rock chemical analyses were performed at BUREAU VERITAS (Canada), using lithogeochemical lithium borate fusion for REEs, and lithium borate fusion LA-ICP-MS for whole-rock analysis. The results are provided in Table 1. The dioritic sample M7A displays negative Loss on Ignition (LOI) values due to the oxidation of Fe²⁺ to Fe³⁺(Sababa *et al.* 2021; Vandenberghe *et al.* 2010) during high-temperature ignition at 1000–1050°C.

The samples were investigated for microstructures and mineral composition by Scanning Electron Microscopy (SEM) using the Quanta 250 equipment at the Nature Research Centre in Vilnius, Lithuania. The chemical composition of rock-forming minerals (as presented in Supplementary Materials from 1 to 5) was obtained by the Energy Dispersive Spectrometry (EDS) detector X-Max, the INCA x-stream digital pulse processor, and the INCA Energy EDS software. The X-Max (large area) 20 mm² silicon drift detector (SDD) is liquid and nitrogen-free. The chemical composition was measured at an accelerating voltage of 20 kV at a current of 1.1–1.2 nA.

Apatite, mica, feldspar, sulphide, ironoxides, titanite, and thorite were analysed using a Cameca SX 100 Electron Microprobe Analyser (EMPA) at the Laboratory of Electron Microscopy, Microanalysis and X-Ray Diffraction, Faculty of Geology, University of Warsaw, Poland (results presented in Supplementary Materials from 6 to 9). The analytical conditions, calibration standards, and element-specific detection limits (in ppm) are detailed in Supplementary Material 10.

Raman spectroscopy analyses and mapping were performed using a Renishaw in Via Qontor confocal Raman microscope at the University of Warsaw. A 532 nm laser was employed in confocal mode with a 50× objective and a motorised XYZ stage to enable high-resolution mapping. Spectra were collected in the range of 100–1870 cm⁻¹ with a spectral resolution of approximately 1 cm⁻¹. Data acquisition and processing were conducted using Renishaw WiRE software. Mineral identification was supported by comparison with reference spectra from the RRUFF database and internal spectral references collected by the University of Warsaw, Faculty of Geology. Raman spectra and reflected-light images of the analysed spots are presented in Supplementary Material 11.

Abbreviations of mineral names used in figures and tables follow the standard recommended by Whitney and Evans (2010).

Table 1 Whole-rock major element (wt%) and trace element (ppm) composition of the studied samples

Wt% /sample	M7A diorite	M7C pegmatitic granite	M7E leucocratic plagiogranite
SiO ₂	47.31	77.46	78.86
Al_2O_3	15.53	13.89	15.51
Fe ₂ O ₃	13.32	1.08	1.26
MgO	6.92	0.34	0.18
CaO	7.01	2.5	3.38
Na ₂ O	3.64	4.1	5.3
K ₂ O	2.94	2.26	0.79
TiO,	1.82	0.31	0.15
P ₂ O ₅	0.63	0.02	< 0.01
MnO	0.29	0.02	0.02
Cr ₂ O ₃	0.036	< 0.002	< 0.002
LOI	0.2	-2.2	<-5.1
Sum	99.68	99.87	99.92
Ppm			
Ba	188	369	102
Ni	97	< 20	< 20
Sc	30	< 1	< 1
Be	9	3	4
Co	35.1	1.1	0.5
Cs	2	0.3	< 0.1
Ga	24.7	16.7	18.1
Hf	3.7	4.3	5.7
Nb	35.3	32.2	11.1
Rb	206.6	66.5	23.6
Sn	7	< 1	< 1
Sr	169.3	217.1	188.1
Та	1.5	2.8	0.9
Th	7	171.4	43.3
U	2.6	40.6	6.4
V	197	10	17
W	0.8	< 0.5	0.8
Zr	157.6	134.1	211
Y	74.3	45.5	19.2
La	35.9	26.6	9.2
Ce	104	54.6	22.3
Pr	15.88	8.57	3.37
Nd	61.9	36.4	14.4
Sm	12.81	7.85	3.19
Eu	2.48	1.03	0.62
Gd	11.46	7.29	3.02
Tb	1.93	1.14	0.46
Dy	12.19	7.18	2.94
Но	2.62	1.55	0.61
Er	8.31	4.67	1.78
Tm	1.35	0.7	0.27
Yb	9.4	4.42	1.7
Lu	1.47	0.65	0.26
F	6547	282	189

RESULTS

Sample description

Three samples collected at the contact zones were selected for a detailed investigation: M7A, M7C, and M7E. Whole-rock major element and trace element compositions of these samples are represented in Table 1. Thin sections gained from these samples exhibit diverse mineralogical and geochemical overprints, including feldspar albitisation, breakdown of titanite and biotite, and the formation of secondary carbonates, barite, and REE-bearing phases. Sample M7E also preserves two texturally and chemically distinct generations of titanite.

Sample M7A (depth 293 m)

This sample represents a contact between a weakly gneissic melanocratic diorite and a massive, coarse-to very coarse-grained granite. The contact is irregular and characterised by mineralogical and textural transitions over a few centimetres.

Dioritic part of sample M7A. The melanocratic, sub-equigranular to slightly porphyritic diorite M7A is composed of amphibole ca. 40%, plagioclase ca. 25%, biotite ca. 25%, and quartz ca. 3%. Accessory minerals include apatite, magnetite, hematite, and titanite. A weak foliation is defined by the preferred alignment of amphibole and biotite (Fig. 2A).

Amphibole is the dominant mafic mineral, occurring as subhedral to euhedral prismatic, 0.3–1.2 mm long crystals. It is homogeneous, with weak undulous extinction and locally developed simple twinning. Most grains show sharp grain boundaries against plagioclase or quartz, although some exhibit curved contacts or intergrowths with biotite.

Plagioclase occurs as subhedral to anhedral tabular grains, ranging from 0.2 to 1.0 mm in length, and displays well-developed polysynthetic twinning. The BSE images are homogeneous or weakly oscillatory-zoned (Fig. 2B). Grain boundaries are generally sharp, although minor replacement by albite is observed near the contact with granite. Myrmekitic textures are absent in the diorite itself but appear in transitional zones toward the granite contact.

Biotite grains are commonly aligned sub-parallel to amphibole and plagioclase, contributing to the weak gneissic texture of the diorite (Fig. 2A). Subhedral to euhedral laths and flakes of biotite, typically ranging from 0.2 to 1.0 mm, are often intergrown with amphibole (Fig. 2B). Some flakes are bent, weakly altered, with localised replacement along cleavage planes by fine-grained Fe-rich chlorite. No significant reaction rims or alteration halos are observed, contrasting with the more altered biotite textures near the granite contact. Quartz occurs as interstitial anhedral grains (< 0.3 mm), showing weak undulous extinction and no recrystallisation textures.

The rock is rich in accessories: apatite, magnetite, and titanite. Euhedral to subhedral prismatic apatite crystals (20–100 μm) are commonly included in amphibole and plagioclase and are homogeneous in the BSE images. Subhedral to anhedral grains (50–200 μm) of magnetite commonly occur along grain boundaries (Fig. 2B). Titanite forms small subhedral grains (0.2–0.4 mm), typically with diffuse outlines and internal fractures (Fig. 2C). Chlorite and calcite occur as minor secondary phases found in microfractures and alteration halos around biotite and amphibole, and in association with altered titanite and microveins, respectively.

Leucocratic granitic part of M7A. This rock is

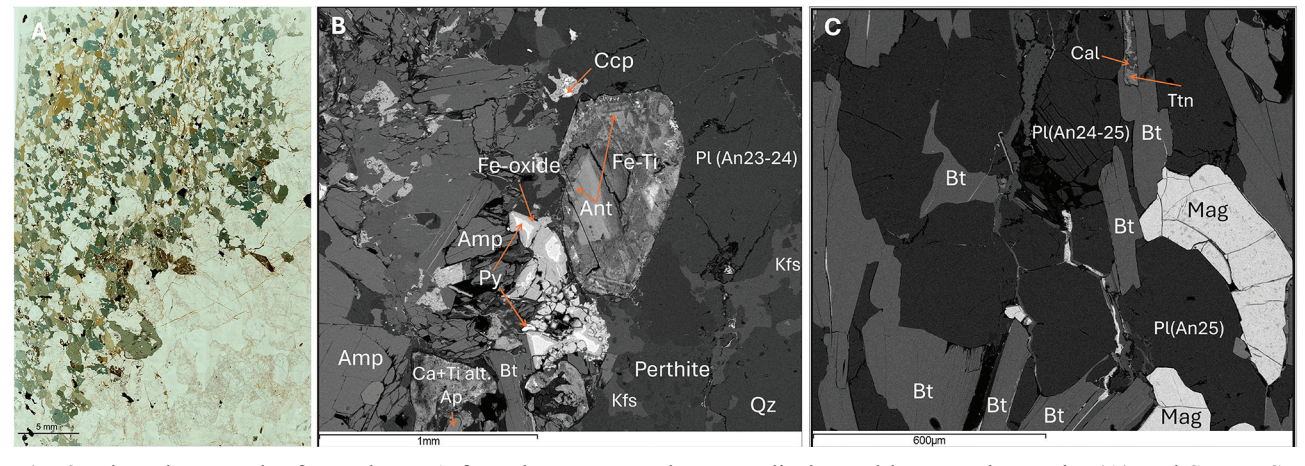


Fig. 2 Microphotograph of sample M7A featuring a contact between diorite and leucocratic granite (A) and SEM BSE images of sample M7A: Sulphide-rich zone near the contact. Amphibole occurs with biotite and plagioclase. Sulphides (pyrite, chalcopyrite) are intergrown with Fe-oxides and anatase along grain boundaries. Ca – Ti-rich alteration phases fill microfractures and interstitial spaces (marked Ca + Ti alt. in Fig. 2B), representing porous secondary domains enriched in Ca and Ti. K-feldspar shows perthitic textures near quartz (B); a fresh dioritic domain illustrating unaltered magnetite grains enclosed in biotite and plagioclase. Titanite occurs in association with calcite within fractures of plagioclase and likely represents a secondary phase formed from Ti mobilisation during biotite alteration (C)

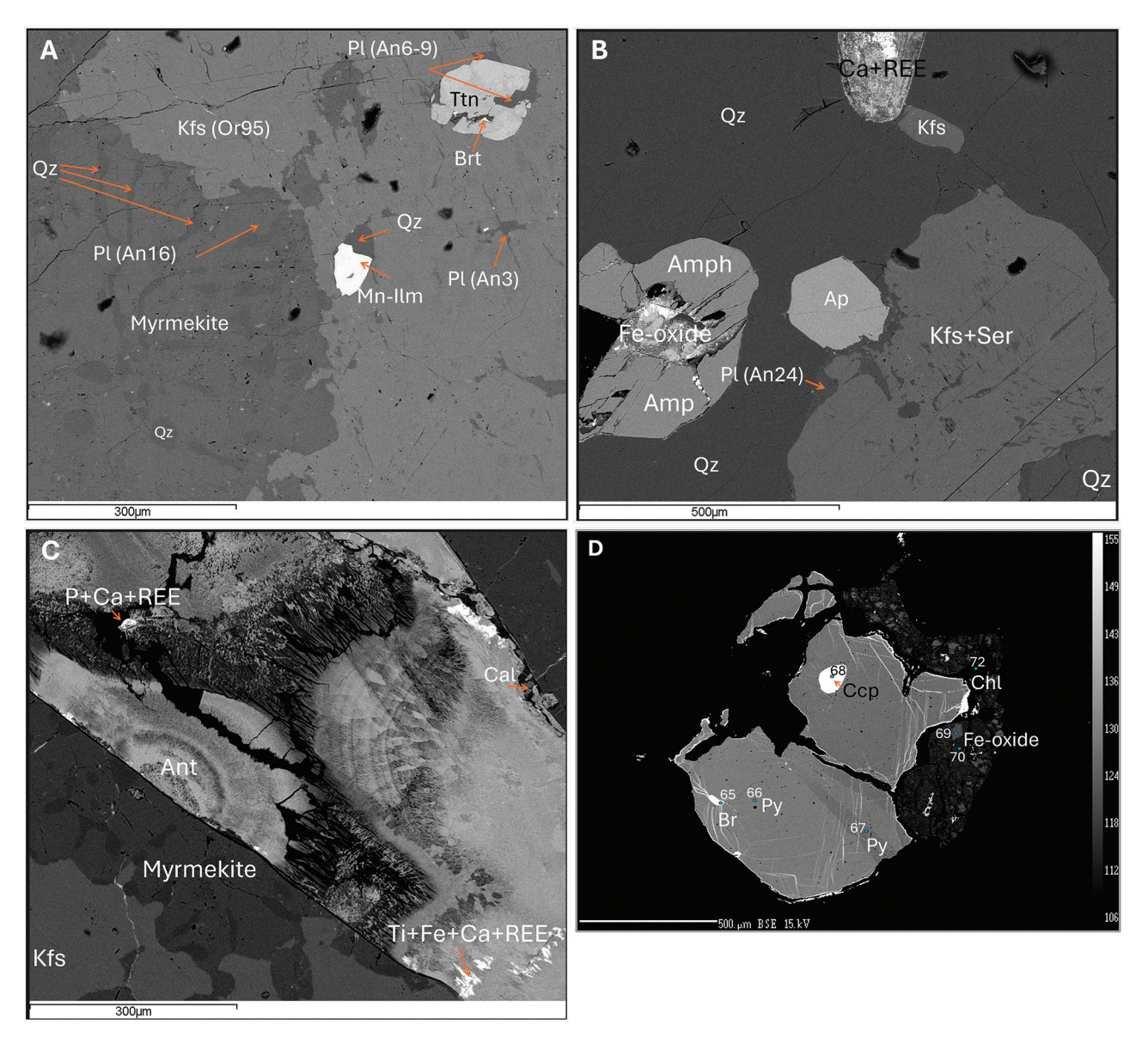


Fig. 3 SEM BSE images of leucocratic granite (A, B) and titanite assemblages (C, D) from sample M7A: myrmekitic intergrowths along albite – K-feldspar boundaries in leucogranite. Note the weakly altered titanite inclusion in K-feldspar, upper right corner (A). Mn-rich ilmenite, titanite, and barite are observed within plagioclase (An₃-₁₆). Amphibole xenocryst near the contact, enclosed in quartz and K-feldspar, associated with Fe-oxide inclusions and apatite. Note the presence of secondary sericite and Ca–REE phases (B). Strongly altered titanite grain displaying dissolution textures, partially replaced by anatase, calcite, and secondary REE phases. Myrmekitic textures are observed at the grain boundary with K-feldspar (C). BSE EPMA image of a sulphide assemblage composed of pyrite, bornite, chalcocite, and Fe-oxides. Spot numbers correspond to microprobe analyses presented in Supplementary Material 9 (D)

heterogeneous, coarse- to very coarse-grained, and it consists mainly of plagioclase ca. 45%, K-feldspar ca. 25%, and quartz ca. 30%, with subordinate biotite and accessory phases. Alteration intensity increases toward microfractures and near the contact with diorite

Plagioclase is present as subhedral to anhedral grains, ranging in size from 0.5 to 2.5 mm (Fig. 3A). Albitisation is widespread, especially along grain rims and fractures. Albite commonly forms thin rims or irregularly replaces plagioclase along boundaries with K-feldspar. Myrmekites develop along albite-K-

feldspar contacts and are common in strongly altered areas (Fig. 3C; Supplementary Material 2A). K-feldspar occurs as anhedral grains with typical microcline twinning and perthitic exsolution textures. Perthite is coarse and patchy, often accompanied by partial replacement by albite. Biotite is rare and often partially to completely replaced by chlorite or muscovite in some places. Chlorite is fine-grained, Fe-rich, and commonly aligned along former biotite cleavage planes. A single amphibole grain in the granite is found near the contact with the diorite and is probably a xenocryst (Fig. 3B).

Titanite is the most abundant accessory mineral. It occurs as large (0.5–1.5 mm), subhedral to anhedral grains with porous textures. Many grains are fractured and partially replaced by anatase and calcite, especially near contact with diorite (Fig. 3C).

magnetite and secondary hematite. Magnetite grains (0.2–0.8 mm) are subhedral and have reaction rims of hematite (Supplementary Material 4B). Several Mnrich ilmenite grains are presented. Secondary barite fills interstitions in titanite grains or occurs along fractures, often in contact with Ba-rich K-feldspar. There are minor sulphides, occurring as intergrowths of pyrite with chalcopyrite, and bornite (Fig. 3D, 9). Fe-oxide Fe-oxide Bt Pl (An24 Pl (An8) 5 mm 300µm Pl (An23-25) D C Bt Fe-oxide Ttn Pl (An23-24) Ca+REE Hem Kfs (Or96) Pl (An1) Chl Qz Ca+REI Ttn Thr Aln Ant Pl (An16) 300µm

Sulphides such as pyrite, bornite, and chalcocite are

present in microfractures or disseminated throughout

the rock. Pyrite is euhedral; chalcocite occurs as fine

intergrowths with barite and along feldspar cleavage

planes (Fig. 2C). Iron oxides occur both as primary

Fig. 4 Microphotograph of sample M7C (A), SEM BSE images of the same sample: Biotite hosting Fe-oxide alteration products, with exsolution of chlorite, quartz, and zoned plagioclase (from An_{24} in core to An_8 in rim); precipitation of anatase (B). Altered domain with clustered accessory minerals: titanite, barite, Fe–Ti oxides, Ca–REE phases, anatase, and hematite, associated with plagioclase (An_{16-25}), chlorite, and muscovite (C). Biotite replaced by Fe-oxides and in contact with plagioclase (An_{1-24}), K-feldspar (Or_{96}), allanite, and thorite (D)

Sample M7C (depth 304.5 m)

This sample represents a medium- to very coarsegrained leucocratic granite trending into pegmatite. The transition is gradational, with progressive coarsening and changes in accessory minerals (Fig. 4A).

Leucocratic granitic part of M7C. This rock is coarse equigranular and contains ca. 35% K-feldspar, ca. 35% plagioclase, ca. 20% quartz, and ca. 3% biotite (Fig. 4A).

Plagioclase grains have polysynthetic twinning and weak zoning. Many grains show albitisation, particularly in the contact zone. Albite alteration is associated with calcite, muscovite, and Fe-rich chlorite. A zone near the contact shows saussuritisation of oligoclase, with fine-grained chlorite and calcite occurring along fractures. K-feldspar is represented by microcline. Grains often contain Na-enriched patches. Perthitic textures are common. Quartz forms subhedral to anhedral grains with undulatory extinction, ranging from 0.3 to 1.2 mm in size. It is interstitial and occasionally embays feldspars. Biotite occurs both as fresh, subhedral flakes and as altered grains rimmed or replaced by chlorite (Fig. 4B). Biotite decomposition is marked by blubs of quartz rimmed by Fe-oxides and fine iron streaks (Fig. 4B).

Accessory minerals are zircon, titanite, and iron oxides. Zircon occurs as well-preserved to slightly metamict grains, commonly included within biotite and near titanite (Fig. 4C). Titanite is strongly altered, with original rhombic grains partially preserved but largely replaced by anatase, calcite, and iron oxides (Fig. 4C). Secondary muscovite commonly grows in proximity to decomposed titanite (Fig. 4C).

Iron oxides include hematite and magnetite, with goethite present in altered zones, particularly near biotite and titanite (Fig. 9AB; see Results of Raman spectroscopy). Barite grains are spatially associated with pyrite and calcite, often filling fractures or interstitial spaces. Chlorite and other secondary phases are typically concentrated along fractures, cleavage planes, and in alteration halos.

Accessory phases include barite, uraninite, thorite, and, locally, altered REE-bearing minerals. Allanite associated with thorite, and goethite associated with magnetite and hematite were identified (Supplementary Material 11, Figs 2, 3). These minerals are concentrated in interstitial pockets or fractures and are spatially correlated with secondary muscovite and calcite (Fig. 4C and D).

Very coarse-grained (pegmatitic) part of M7C. This rock occupies the lower part in Fig. 4A and contains larger grains of feldspars and quartz, as well as numerous accessory phases. K-feldspar is represented by nearly pure microcline, with some grains showing minor enrichment in fluorine and traces of barium. Plagioclase is subordinate, consisting of albite and oligoclase, often intergrown with K-feldspar or quartz.

Sample M7E (depth 352.7 m)

This sample represents a contact of medium-grained leucocratic plagiogranite and coarse-grained (pegmatitic) biotite granite (Fig. 5A). Accumulations of quartz occur in the pegmatitic granite. The contact zone is irregular and crosscut by quartz lenses that contain muscovite and calcite. The contact is marked by coarse titanite and magnetite (with some intergrown hematite) grains (Fig. 5A).

Leucocratic plagiogranite part of M7E. This rock consists of ca. 55% plagioclase, ca. 40% quartz, ca. 5% K-feldspar with some perthites, as well as minor biotite and muscovite. Some plagioclase grains exhibit rounded dissolution textures toward the contact with pegmatitic granite. Some quartz grains have undulatory extinction.

Pegmatitic biotite granite part of M7E. This rock has a mineral composition of ca. 55% plagioclase, ca. 25% quartz, ca. 5% K-feldspar, ca. 10% biotite. Ore minerals, along with zircon, secondary epidote, calcite, muscovite, and chlorite, are concentrated in localised zones near the contact with the pegmatitic granite, forming less than 5% of the overall rock volume.

Plagioclase shows a range from oligoclase to al-

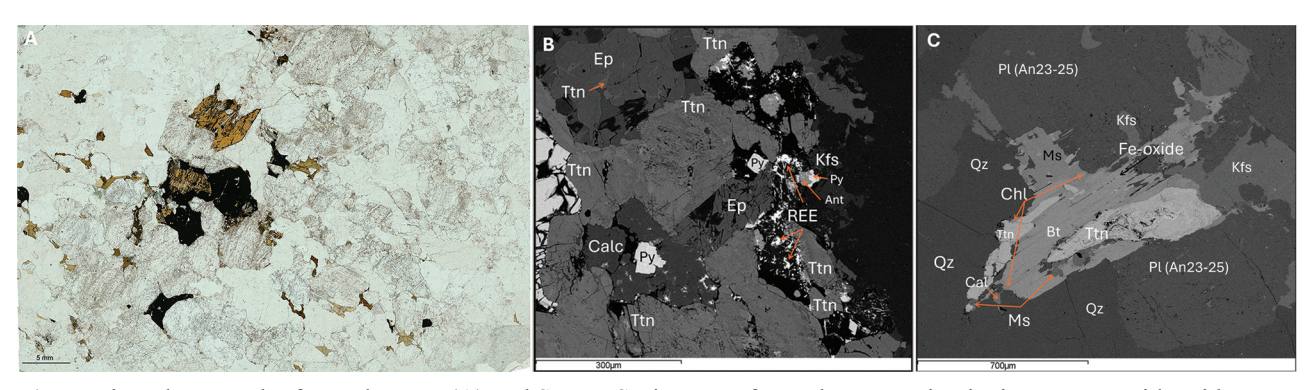


Fig. 5 Microphotograph of sample M7E (A) and SEM BSE images of sample M7E: Titanite intergrown with epidote, pyrite, K-feldspar, calcite, REE-rich phases, and accessory anatase (B). Elongated titanite associated with Fe-oxide, biotite, chlorite, muscovite (C)

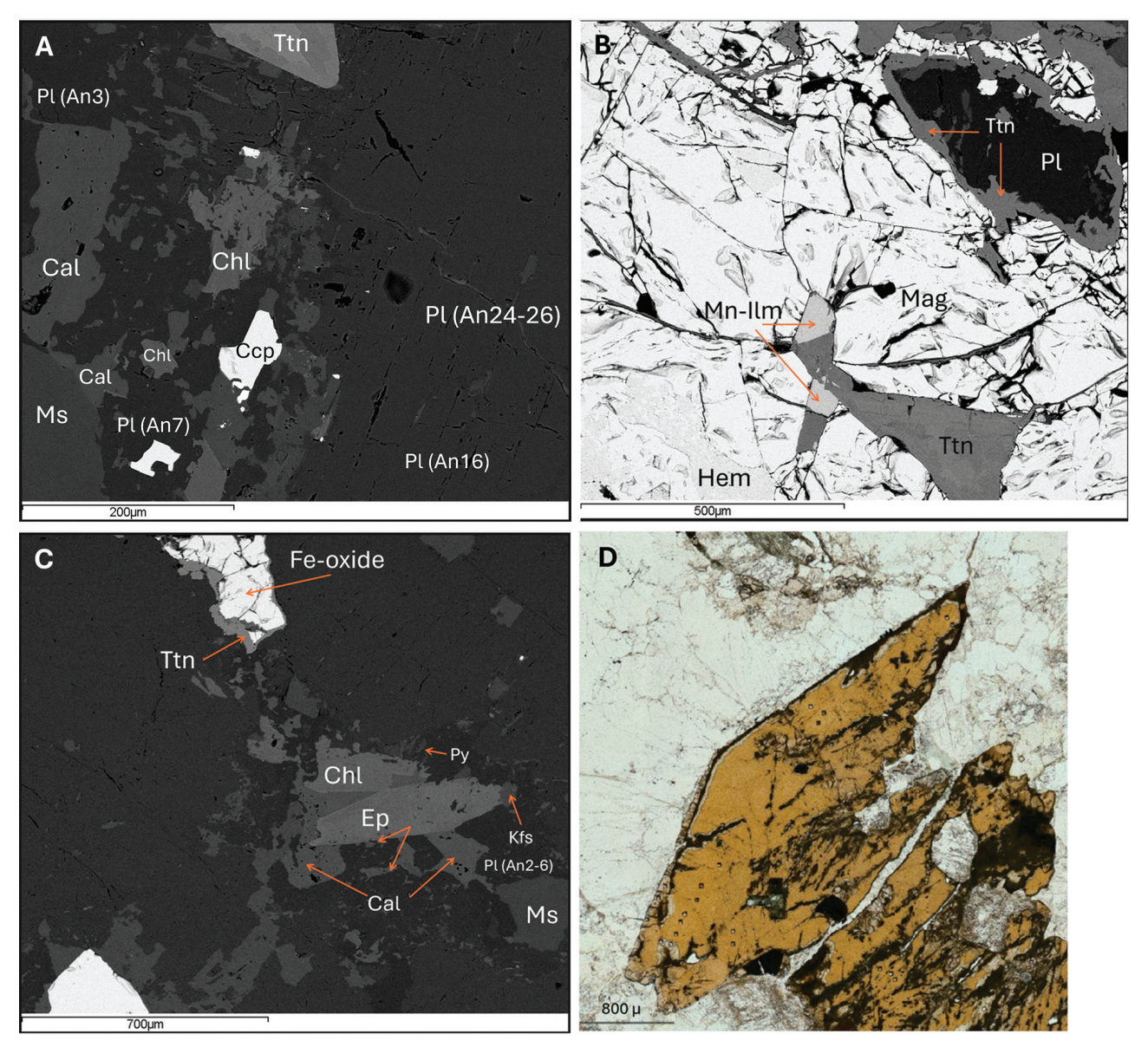


Fig. 6 SEM BSE images (A–C) and plane-polarised light image (D) of sample M7E: Zoned plagioclase (oligoclase in the right part and albitite zone in the left part) with chlorite, muscovite, calcite, titanite, and chalcopyrite (A). Fe-oxide cluster: Mn-rich ilmenite, magnetite, and hematite; titanite rim on magnetite in centre plagioclase oligoclase (B). Altered domain: Fe-oxide grain is rimmed by titanite. Within the plagioclase matrix, K-feldspar, epidote, and muscovite are present, adjacent to albite, forming irregular boundaries with secondary chlorite and calcite (C). Large, euhedral titanite (D)

bitised compositions, with alteration accompanied by calcite, epidote, muscovite, and chlorite formation. K-feldspar occurs as anhedral microcline with signs of dissolution.

Two biotite populations are recognised: first, subhedral flakes enclosed by feldspar and quartz that are compositionally pristine, and second, altered grains replaced by chlorite, typically along fractures, and commonly bordered by dark reaction rims. Irregular muscovite flakes also replace biotite with chlorite.

Titanite occurs in two distinct types. Well-preserved titanite of the first type forms euhedral to subhedral grains reaching up to 4.5 mm, often of rhombic habitus (Fig. 6A, 6D). Grains of the second type are smaller (0.3–0.8 mm), irregular, and display corro-

sion (spongy) textures (Fig. 5B, 5C, 6B, 6C). These second-type titanite grains are disintegrating and being replaced by anatase, magnetite, and calcite. Magnetite is found either as subhedral large crystals up to 4 mm in association with titanite and biotite or fills grain interstices (Fig. 6B; Supplementary Material 4, 7B). Magnetite grains at margins and near fractures are partially altered to hematite (Fig. 6B). Zircon is present as small, euhedral grains, commonly associated with titanite and biotite.

Calcite occurs in areas of secondary alteration together with chlorite, epidote, and albite, or as a replacement product after the titanite. Epidote forms small grains together with other secondary alteration products (Fig. 5B).

Mineral chemistry

Primary silicate minerals

Plagioclase compositions in the dioritic part of sample M7A range from An₂₃ at rims to An₂₅ at cores (Fig. 2B, C; Supplementary Materials 2A). In the leucocratic granitic part of M7A, plagioclase shows a broader range, from An₁ to An₂₅, with local albitisation near contacts and fractures (Fig. 3A, B; Supplementary Materials 2A) and evidence of saussuritisation near the contact zone (Supplement 2A, 5). In the leucocratic granitic part of M7C, plagioclase varies from An₁₀ to An_{25} , with albitisation reducing compositions to An_{1-8} near contact zones (Fig. 4B; Supplementary Materials 2B). In the pegmatitic part of M7C, plagioclase consists of albite and oligoclase, ranging from An, to An, (Fig. 4; Supplementary Material 2B). The leucocratic plagiogranite of M7E shows oligoclase compositions from An₁₁ to An₂₅ (Fig. 5; Supplementary Material 2C), while in the pegmatitic biotite granite of M7E, plagioclase also shows gradual albitisation (Figs 5, 6; Supplementary Material 2C).

K-feldspar is represented by microcline, and perthitic textures are common in granitic and pegmatitic domains, with the most evolved compositions (lowest An, highest Or) in the pegmatitic zones, consistent with progressive differentiation. Minor F and Ba incorporation in some K-feldspar grains suggests limited fluid-related element enrichment. K-feldspar in the leucocratic granitic part of M7A has compositions between Or_o, and Or_{96} , with a slight albitic shift $(Or_{88}-Or_{93})$ near the diorite contact. Some grains contain up to 0.01 atoms per formula unit (apfu) of Ba (Fig. 2; Supplementary Material 2A). In M7C, K-feldspar is represented by microcline with compositions from Or_{92} to Or_{96} in the leucogranitic part and from Or₇₂ to Or₉₆ in the pegmatitic part (Fig. 2; Supplementary Material 2B). In M7E, K-feldspar shows compositions from Or_{95} to Or_{97} in the leucocratic plagiogranite and is anhedral, dissolved microcline in the pegmatitic biotite granite (Fig. 5; Supplementary Material 2C). These compositional ranges are illustrated in the Or-Ab-An ternary diagram (Fig. 7A).

Amphibole occurs only in the dioritic part of sample M7A, while the leucocratic granitic part contains just a few xenocrysts. With Mg# values between 49 and 50 and titanium contents ranging from 0.08 to 0.11 (apfu), amphibole from the dioritic part is classified as magnesio-hastingsite (Fig. 7B; Supplementary Material 1).

Biotite in the dioritic part of M7A shows Fe# values of 37–40, Ti from 0.14 to 0.25 apfu, Cl from 0.01 to 0.09 apfu, and F from 0.61 to 1.18 apfu (Supplementary Material 3A), with core-to-rim zoning expressed by higher Fe and Mg in cores and lower F in rims. In the leucocratic granite of M7A, biotite is altered and occurs as irregular flakes with Fe# values of 41–42 and Ti contents between 0.20 and 0.23 apfu. Cl from 0.13 to 0.19 apfu, and F from 0.98 to 1.06 apfu (Supplementary Material 3A). Biotite from the leucocratic part of M7C has Fe# values of 43-47, Ti 0.23-0.33 apfu, with Cl between 0.05 and 0.13 apfu and F ranging from 0.73 to 1.57 apfu (Supplementary Material 3B). In the pegmatitic biotite granite of M7E, two groups are observed. First, altered biotites with Ti contents of 0.26–0.32 apfu and Fe# values of 49-61, Cl 0.10-0.12 apfu, F up to 0.85 apfu, and second, nearly unaltered grains with Ti contents of 0.20–0.22 apfu and Fe# values of 44–45, Cl 0.09–0.14 apfu, and F up to 0.79 apfu (Supplementary Material 3C). In addition, one analysis represents biotite in direct contact with chlorite, showing a Fe# value of 51 and Ti content of 0.19 apfu with Cl 0.11 apfu and F below detection limits.

The ternary diagram (MgO–FeO + MnO–TiO $_2 \times 10$) illustrates the compositional variation of biotite from different varieties of the Marcinkonys-7 sample (Fig. 8A). Most biotites in the ternary diagram (MgO–FeO + MnO–TiO $_2 \times 10$) plot within the field of re-equilibrated biotite field, suggesting pervasive post-magmatic overprint and partial chemical reset-

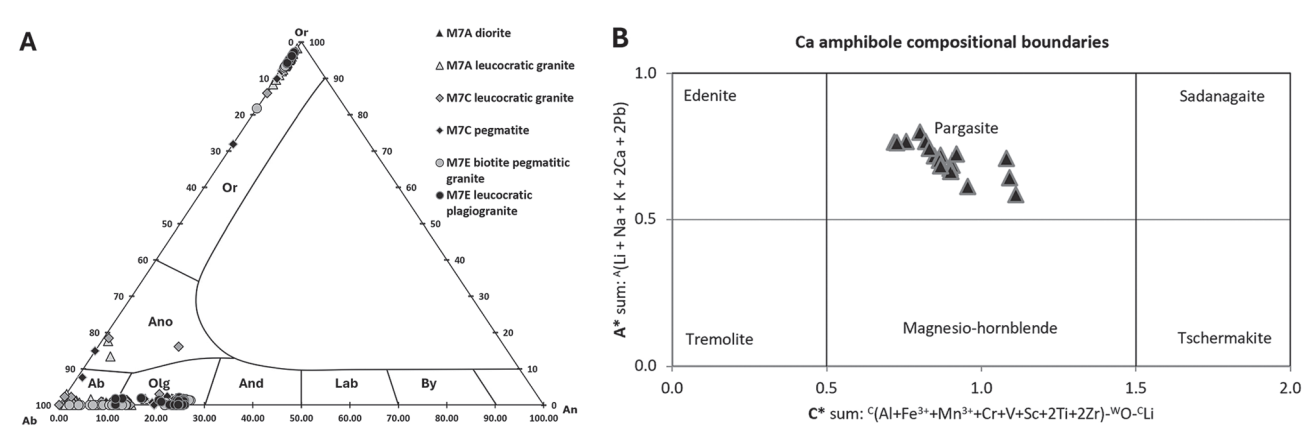


Fig. 7 Feldspar compositions in the Or-Ab-An system after Marshall (1996) (A). Classification of amphiboles from the M7A diorite based on A and C cation sums after Leake *et al.* (1997). All amphibole analyses plot in the pargasite—hastingsite field, but Fe³⁺> Al VI indicates they correspond to hastingsite (B)

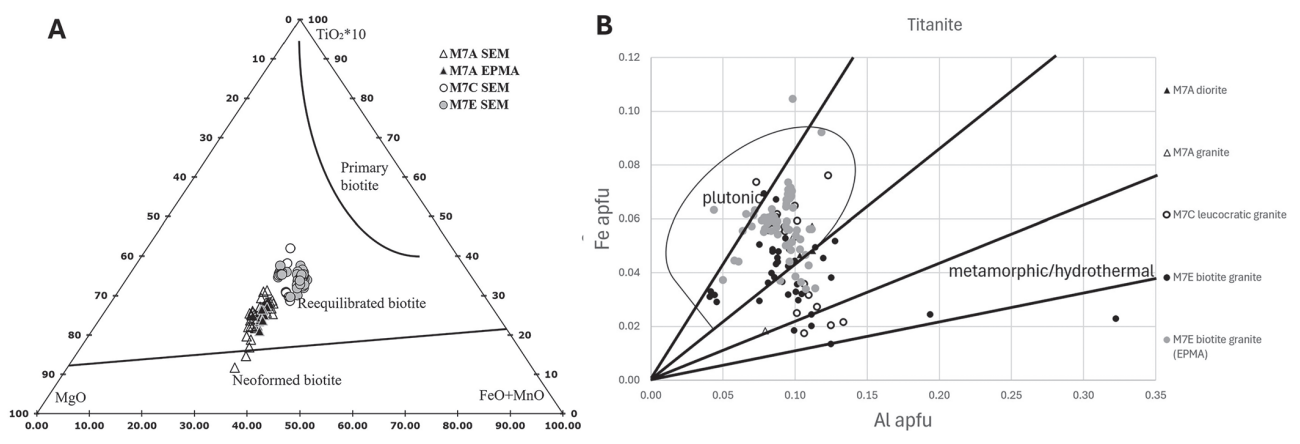


Fig. 8 Compositional classification of biotite in the MgO–FeO + MnO–TiO₂ × 10 system showing primary, reequilibrated, and neoformed fields after Nachit *et al.* (2005) (A). Al-Fe compositional diagram for discriminating magmatic and metamorphic titanite after Kowallis *et al.* (2022) (B)

ting under fluid influence. Notably, two grains near the contact between granite and diorite from the M7A sample plot within the neo-formed biotite field. Their composition indicates formation from reactive fluids, likely enriched in Fe and Mg, which facilitated the localised neocrystallisation of biotite in response to metasomatic alteration at the lithological boundary (Nachit *et al.* 2005).

Secondary alteration products

Chlorite chemistry is presented in Supplementary Material 5 – SEM and Supplementary Material 6 – EPMA. The M7A diorite shows a broad range in #Fe from 33 to 74, whereas the M7A granitic part contains uniformly Fe-rich chamosite #Fe = 57–60.

The M7C exhibits the widest compositional range with Fe# from 36 to 97, whereas chlorite from the M7E biotite pegmatite is almost uniformly Fe-rich (#Fe 93–97), with minor core-to-rim increases in tetrahedral Al and decreases in Fe²⁺. The chlorite from sample M7E leucocratic plagiogranite (#Fe = 90–97) is more heterogeneous, with Fe-rich cores and Al-rich rims.

Muscovite across all lithologies shows comparable Si and total Al contents, with the main variations expressed in Fe-Mg proportions and Na levels. Pegmatite M7E muscovite shows elevated Mg in rims relative to cores (Supplementary Material 5), whereas granite M7C muscovite shows smaller rimcore differences but similar Mg enrichment in rims. Granite M7A muscovite is generally Mg-poor (up to 0.20 apfu) with variable Fe (0.38–0.93 apfu) and minor rim–core variation. Ti in M7A is low (up to 0.03 apfu), while in M7C and M7E, Ti is up to 0.07 apfu.

Apatite dioritic part of sample M7A grains is fluorapatite in composition, with F contents ranging from 1.77 to 2.62 apfu, Cl from 0.03 to 0.09 apfu, and minor Fe up to 0.06 apfu (Supplementary Material 4A). Titanite occurs as subhedral grains with Ti contents of 0.86 apfu, F contents of 0.13–0.14 apfu

and shows weak LREE enrichment (Supplementary Material 4B).

Titanite rims in M7A are enriched in Ti (0.91 apfu) relative to cores (0.84-0.85 apfu), with Fe/Al ratios dropping from 0.51-0.54 to 0.23 (Supplementary Material 4), reflecting Fe loss and Ti gain during late-stage alteration. Ti contents in M7A show a broader scatter compared to other domains, indicating more pronounced compositional variability. In M7C, the pegmatitic part shows relatively homogeneous Ti contents (0.85–0.87 apfu) with only minor scatter, low Fe^{2+} (0.02–0.03 apfu), and low Fe/Al (0.16–0.29), indicating minimal post-crystallisation modification. The leucogranitic domain of the same sample displays mild zoning, with a slightly broader Ti range (0.83-0.89 apfu) and similar low Fe/Al ratios, suggesting limited alteration compared to M7A. Titanite in the M7E biotite pegmatite shows similar variation in Ti content (0.84–0.93 apfu) and a subtle rim enrichment in F (up to 1.8 wt%) and REE (La up to 1.3 wt%; Supplementary Material 4, 7B). The Al–Fe diagram for titanite distinguishes between igneous and metamorphic/hydrothermal origins based on Fe/Al ratios (Fig. 8B; Kowallis et al. 2022). Most analyses from the Marcinkonys-7 samples plot within or near the "plutonic" field, consistent with magmatic titanite. Notably, titanite grains marked with filled grey circles (M7E biotite granite) fall within the field of unaltered igneous titanite, exhibiting Fe/Al ratios close to 1:1 and well above the 1:2 threshold, supporting their primary magmatic origin and minimal post-crystallisation alteration.

Zircon from the leucocratic granitic part of M7C contains 0.97–0.99 apfu of ZrO₂ and 0.01–0.02 apfu of HfO₂; one point contains 0.01 apfu of UO₂ (Supplementary Material 4F).

Oxide and sulphide minerals

Iron oxides. All analysed Fe-oxide grains from M7A and M7E yield $Fe^{2+}/(Fe^{2+} + Fe^{3+})$ ratios of 0.34

and totals close to the stoichiometry of magnetite, with Ti contents ranging from below detection limit to 0.05 apfu (Supplementary Material 7A). These values indicate compositions corresponding to magnetite—titanomagnetite solid solutions. In addition to Ti, the grains contain minor Cr (up to 0.03 apfu), V (up to 0.05 apfu), Al (up to 0.05 apfu), and Mn (up to 0.03 apfu), with occasional traces of Ca, Ni, and Co. No evidence for a hematite end-member was detected by EMPA.

Anatase from the leucocratic granitic part of M7A contains high TiO_2 (0.94 apfu), with notable amounts of Fe_2O_3 (0.03 apfu), Nb_2O_5 (0.01 apfu), CaO (0.01 apfu), and minor REE oxides (Ce_2O_3 0.2 wt%, Y_2O_3 0.05 wt%; Supplementary Material 7C).

Sulphides from M7A are mainly pyrite, which contains up to 0.2 wt% Co. Bornite, found as inclusions in pyrite, contains minor traces of Pb (up to 0.03 wt%; Supplementary Material 9). Chalcopyrite, present in isolated inclusions within altered areas, shows detectable Pb (up to 0.11 wt%). These sulphides occur as fine disseminations, fill microfractures, or are intergrown with barite and calcite, especially in altered zones along feldspar cleavage planes (Fig. 2B; Supplementary Material 9). Pyrite usually forms euhedral grains, while bornite and chalcopyrite appear as irregular inclusions or interstitial grains, indicating fluid-induced redistribution of Cu–Fe sulphides.

Barite from the leucocratic granite (M7C, Fig. 4C) is spatially associated with pyrite and calcite. It has low amounts of CaO (up to 2.5 wt%), suggesting limited Ba-Ca substitution. FeO is typically low (0.3–0.9 wt%). Traces of SiO₂ and Al₂O₃ are present in some grains, while other elements remain below detection limits (Supplementary Material 4C).

Biotite thermometry

Henry *et al.* (2005) presented a geothermometric expression based on Ti content in biotite. In the M7A dioritic domain, biotite contains from 0.18 to 0.25 apfu Ti and yields Ti-in-biotite temperatures of 608–660 °C (Supplementary Material 3A). Titanite adjacent to the alteration zone is replaced by anatase, and Fe-oxide filled cracks, biotite shows lower Ti contents (0.14–0.16 apfu, corresponding to 550–590 °C), whereas the leucocratic part of the M7A granite shows 0.20–0.23 apfu and higher temperatures (ca. 620–640 °C).

In M7C, biotite contains the highest Ti (up to 0.33 apfu) and records temperatures of ca. 640–690 °C, with one point in the core of the grain having relatively low 0.23 apfu Ti and a lower temperature of ca. 620 °C (Supplementary Material 3B). In the pegmatitic domain, biotite in inclusion shows locally elevated Ti (0.34 apfu) with the highest recorded temperatures (700 °C).

Biotite from the M7E biotite granite records Ti

contents of 0.24–0.32 apfu and temperatures of ca. 630–680 °C. Two points from the inner part of the biotite with lower Ti (0.19–0.20) content yielded lower temperatures: one point near chloritisation (Ti 0.19 apfu; 580 °C), and one point near intergrowth with newly formed titanite (Ti 0.20 apfu; 610 °C) (Supplementary Material 3C). The leucocratic plagiogranite contains biotite with Ti 0.24 apfu and temperatures around 630 °C.

Ti-in-biotite thermometry yielded temperatures in a range of 700–620 °C for the more Ti-enriched biotite varieties and slightly lower temperatures from more altered biotite. Biotite inclusions in pegmatite (M7C) record the highest temperatures.

Results of Raman spectroscopy

Raman spectroscopy was used to identify fine-grained and compositionally ambiguous mineral phases that were difficult to resolve by optical microscopy or SEM-EDS alone. Analyses were performed on selected areas in samples M7A and M7C. These results confirm the presence of hematite, magnetite, goethite, allanite, anatase, barite, and chalcopyrite across several alteration zones. In sample M7A, Raman spectroscopy confirms the presence of chalcopyrite based on its spectral match with reference mate-

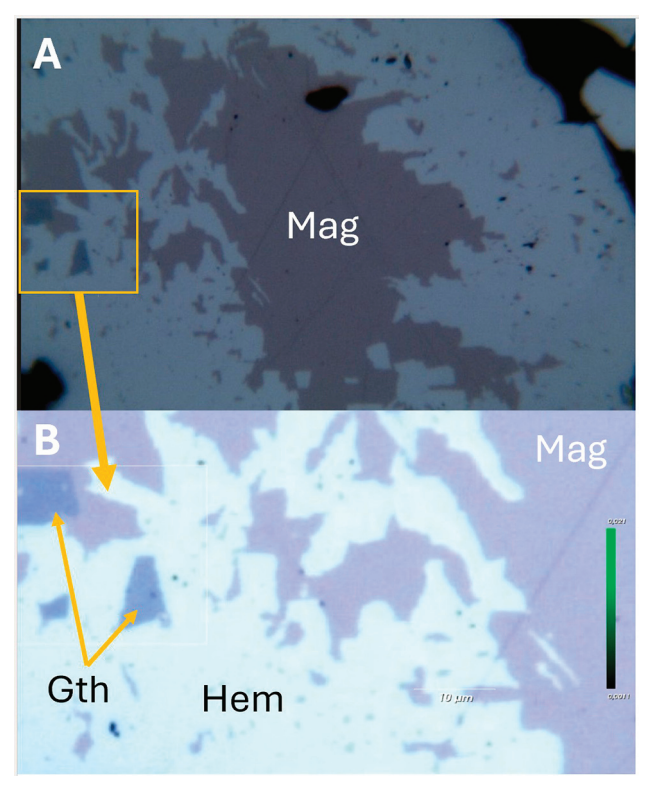


Fig. 9 Reflected light images and Raman spectra illustrating iron oxide mineralisation in sample M7C (leucocratic granite). Central magnetite grain surrounded by secondary hematite and minor goethite (A). Closer view of grain margins showing transitions from magnetite to hematite and goethite (B)

rial (Supplementary Material 11, Fig. 1). In sample M7C, Raman spectra from iron oxide grains (Fig. 9 and Supplementary Material 11, Fig. 2) reveal distinct mineralogical zonation. The magnetite cores exhibit a strong peak near 665 cm⁻¹, while the surrounding rims display characteristic hematite bands at ~225, 245, 295, 410, 500–610, and a two-phonon band near 1320 cm⁻¹. Locally, weak bands in the 300–500 cm⁻¹ region indicate the presence of goethite. No spectral evidence of magnetite or Fe–Ti oxide phases is detected in the outer zones.

Another analysed area within the leucocratic granite portion of sample M7C shows a mineral with peaks in the 160-600 cm⁻¹ range and a broad band near 1200–1500 cm⁻¹, consistent with allanite (Supplementary Material 11, Fig. 3). The same phase was previously described petrographically (Fig. 4D) near thorite grains and occurs adjacent to isotropic phases and secondary silicates. In the same locality, anatase was identified by diagnostic peaks typical of TiO₂ polymorphs (Supplementary Material 11, Fig. 4), and mapping confirmed its spatial concentration in Ti-rich zones. Barite was identified by its diagnostic Raman peaks at ~ 450, 620, 985, and 1010 cm⁻¹, matching the reference spectrum for BaSO₄. The bright, highrelief barite grains occur as irregular clusters within altered feldspar domains (Supplementary Material 11, Fig. 5).

DISCUSSION

Whole-rock geochemical data were used to evaluate the origin and tectonic setting of the studied rocks. For comparison, average values from nine unaltered and four altered Kabeliai granite samples were used based on the dataset published by Stein et al. (1998). The average of the unaltered Kabeliai granites in Fig. 10A, along with our sample (M7E), plots near the boundary between the peraluminous and metaluminous domains, within the biotite granite field (zone III; Fig. 10A), similar to the most granitic varieties from the Mesoproterozoic Mazury suite farther east (cf. Skridlaite et al. 2003). The alterations described previously (e.g. M7C) enrich the granite composition in alkalis and shift it towards the metalumineous field of the diagram (Fig. 10A). In addition to the granitic and altered samples, one mafic sample (M7A), classified as a diorite based on its low SiO₂ (47.3 wt%, Table 1) and elevated FeO, MgO, and CaO contents, was plotted on the A–B diagram. Its position within the metaluminous domain, with significantly higher B values and low A, is consistent with its mafic composition. The classification diagram for Ca-amphiboles (A* vs. C* cation sums) shows that all amphibole compositions from the dioritic part of sample M7A fall within the magnessio-hastingsite field (Fig. 7B).

Amphiboles in diorite sample M7A were classified as hastingsite, suggesting their formation from K-rich melts (e.g., Dalpe and Baker 2000; Irving and Green 2008; Freise *et al.* 2009) that fractionated to the granitic melt.

The Nb–Y discrimination diagram was used to assess the tectonic setting of the studied samples. The two least altered granite samples (M7A and M7C) plot in the within-plate (A-type) granite field characterised by elevated Nb and Y contents (Fig. 10B). The altered M7E granite plots within the volcanic arc and syn-collision granite field, likely reflecting redistribution or partial depletion of Nb and Y during alteration. Overall, the geochemical data suggest that the studied samples are A-type granites formed in a within-plate tectonic setting, though metasomatic overprint is evident.

The Ti-in-biotite thermometry results yielded temperatures of ca. 620–700 °C, suggesting magma solidification at these conditions. The sequence of mineralogical transformations observed in samples M7A, M7C, and M7E reflects a complex post-

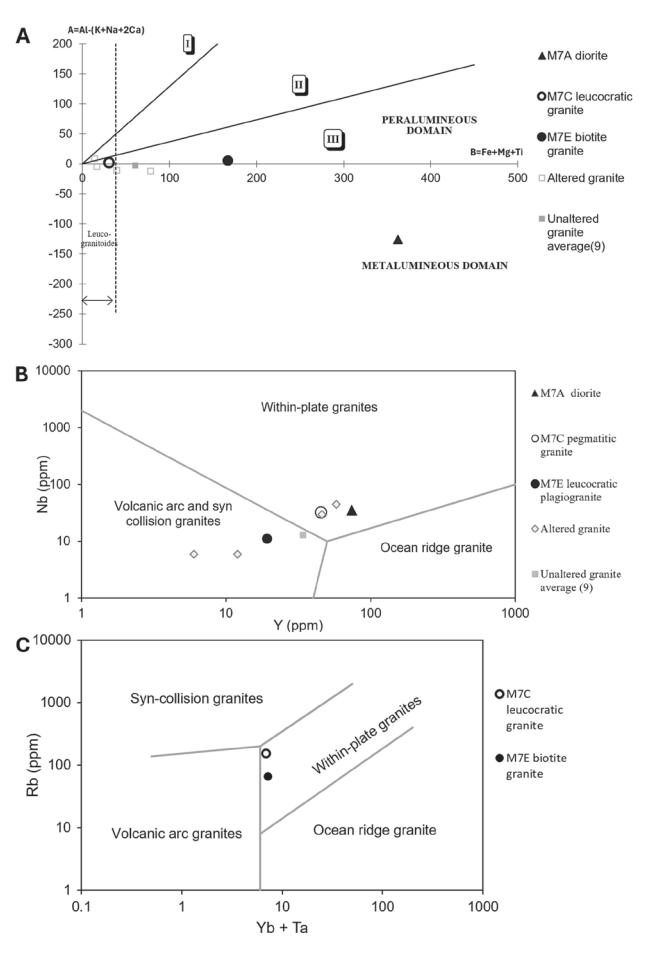


Fig. 10 The Marcinkonys-7 samples plotted on AB diagram after Debon and Le Fort (1983) (A). I–III – fields of granitoid compositions: I – muscovite alone or muscovite > biotite (by volume), II – biotite > muscovite, III – biotite alone. Discrimination diagrams of Nb/Y (B; after Pearce *et al.* (1984)) and of Rb/Yb + Ta (C; after Eby (1992))

magmatic evolution driven by fluid-rock interactions under progressively cooling conditions. Each step corresponds to specific fluid regimes and redox environments, ranging from near-solidus re-equilibration to advanced metasomatic overprint. These transformations, each characterised by distinct mineralogical and geochemical signatures, are described below.

Indications of late-magmatic crystallisation and textural equilibration (pre-alteration phase) can be observed in the studied samples, defined by the formation of unaltered rock-forming minerals such as amphibole, plagioclase, K-feldspar, quartz, and biotite. Titanite is euhedral, and the core is chemically homogeneous with an altered rim (sample M7E, Fig. 6D), as is apatite (sample M7A, Fig. 3B). They reflect stable magmatic crystallisation typical of anorogenic granites, where low deformation rates promote the retention of early magmatic textures (Frost, Frost 2011).

During the later step, subsolidus feldspar re-equilibration and minor metasomatism commence. Feldspars begin to record post-magmatic adjustments. Perthitic textures develop in K-feldspar (Sample M7A, Figs 2B and 3A), and albite rims appear on plagioclase (Figs 3A and 4D), consistent with low-T Na–K exchange. Myrmekitic intergrowths of quartz and albite form along feldspar boundaries. These reactions are likely controlled by closed-system fluid interactions. They are documented in M7C (Fig. 4C) and M7A (Fig. 3C). The incorporation of Ba in K-feldspar and the presence of early anatase suggest incipient fluid involvement (Vernon 2004; Shelley 1993).

The following step is marked by pervasive fluid interaction and hydrothermal overprint by alkali- and sulphate-bearing fluids. Feldspars undergo progressive albitisation, and K-feldspar shows Ba enrichment (Fig. 3A). Biotite is replaced by chlorite and muscovite (Fig. 5C). Among sulphate minerals, only barite was identified in the studied samples. It occurs together with calcite in fractures and altered feldspar zones, indicating a late hydrothermal origin. Titanite develops porous textures and is partially replaced by anatase and carbonates (Figs 2B, 3C, 4C). Magnetite begins to oxidise (Fig. 6B). These features indicate a shift to an open-system regime with oxidising SO₄²⁻ and CO₂-rich fluids, like those described by Feng *et al.* (2023) and Förster (2000).

At the final step, accessory minerals become the focus of alteration. Titanite is pervasively replaced by anatase, REE-bearing calcite (Figs 2B, 4C, 5B). Hematite rims on oxidised magnetite (Fig. 10A, B) and the presence of barite (Fig. 3A) with sulphides support advanced metasomatism under oxidising conditions.

Taken together, the mineralogical evidence suggests two major pulses of fluid activity: an earlier event involving Na- and SO_4^{2-} -rich fluids responsible

for feldspar metasomatism and barite precipitation, and a later pulse involving F–CO₂-rich fluids that overprinted accessory minerals and mobilised trace elements. These events operated along fractures and grain boundaries, resulting in localised but mineralogically intense alteration.

Morad *et al.* (2009) documented analogous textures in Proterozoic granites of south-eastern Sweden, where magmatic titanite underwent dissolution and replacement by anatase and secondary titanite. Their study highlighted that such alteration is associated with albitisation of feldspars, chloritisation of biotite, and hematite formation, a pattern that closely parallels our observations in the studied Marcinkonys-7 samples. These textural and chemical similarities support a model in which accessory minerals serve as sensitive tracers of late-stage hydrothermal processes and further suggest that REE remobilisation in our samples was driven by fluids of comparable composition and redox state.

An important task of this study is to unravel sources and conditions for REE release and accumulation. Titanite is one of the main REE-incorporating phases in Kabeliai granites. Rare earth element mobilisation into and from titanite during fluid-assisted alteration is a well-documented process, where REEs are incorporated or leached depending on fluid composition, temperature, and fO₂ conditions (Xiao et al. 2020). In particular, hydrothermal titanites from alteration zones commonly exhibit significant depletion in total REE contents compared to their magmatic counterparts, reflecting REE partitioning dynamics during successive fluid-rock interaction events. In the studied samples, altered titanite grains often display porous and fractured textures and are partially or fully replaced along rims and cleavage planes. Secondary phases formed during this replacement include anatase, calcite, and REE-carbonates. Similar fluid-driven titanite alteration textures have been described by Middleton et al. (2012). These alteration products are typically associated with increased oxidation (Fe-oxide formation) and albitisation of feldspars (Kontonikas-Charos et al. 2014). Such mineral assemblages suggest interaction with oxidising, F- and CO2-rich hydrothermal fluids capable of remobilising Ti, Ca, and REE (Liu et al. 2025). The co-occurrence of REE-carbonates and barite further supports a model involving oxidised, Fand sulphate-bearing fluids capable of mobilising and reprecipitating REEs in structurally and chemically reactive domains.

CONCLUSIONS

1. The geochemical data suggest that the studied samples exhibit features typical of A-type granites, though metasomatic overprint is evident. Similar

alteration textures, involving partial or complete replacement of magmatic titanite by TiO, phases such as anatase, have been described in hydrothermally overprinted granites (Morad et al. 2009; Middleton et al. 2012). Although titanite is documented as an accessory mineral in A-type granitoids of the Mazury Complex (NE Poland), no instances of anatase formation replacement textures have been reported. However, comparable examples of titanite alteration by TiO, phases, including anatase, are known from Proterozoic granites of south-eastern Sweden (Morad et al. 2009). These transformations are attributed to oxidising hydrothermal fluids and occur along fractures and grain boundaries, often preserving the original grain shapes. Experimental studies further demonstrate that F- and REE-rich fluids can induce dissolution-reprecipitation processes in accessory minerals, promoting REE mobility and secondary phase formation of titanite and associated phases (Gmochowska et al. 2024a, b) also supports such fluid-induced modifications.

- 2. The combined mineralogical and geochemical evidence suggests at least two major pulses of fluid activity: an early event involving Na- and SO₄-rich fluids responsible for feldspar metasomatism, biotite chloritisation, and barite precipitation; and a later event involving F-CO₂-rich fluids, which produced extensive replacement of titanite. These fluids exploited fractures and grain boundaries, leading to the localised yet mineralogically intensive alteration, with accessory phases serving as sensitive tracers of fluid pathways and composition.
- 3. Titanite and apatite are major REE-bearing phases. However, REE contents are low in the unaltered titanites. The late F-CO₂-rich fluids have mobilised REEs into carbonate and phosphate phases (apatite) and accumulated them in the titanite alteration products.

Acknowledgments

The research of Olga Demina was supported by the Nature Research Centre doctoral study funds.

A Nikon Eclipse LV100N POL polarising microscope with an epi-illumination attachment was used at the Nature Research Centre (Lithuania) to investigate mineral textures, microstructures, and alteration patterns. The equipment was purchased as part of the PALEO project funded by the Research Council of Lithuania (LMTLT), agreement No. P-MIP-23-129. Whole-rock chemical analyses were also funded by the Research Council of Lithuania (LMTLT) under the same agreement. We are grateful to Petras Jokubauskas for his valuable help and technical support during the EPMA work. The authors would like to sincerely thank two anonymous reviewers for their helpful feedback and recommendations.

REFERENCES

- Bogdanova, S., Gorbatschev, R., Skridlaite, G., Soesoo, A., Taran, L., Kurlovich, D. 2015. Trans-Baltic Palaeoproterozoic correlations towards the reconstruction of supercontinent Columbia/Nuna. *Precambrian Research* 259, 5–33. DOI: 10.1016/J.Precamres.2014.11.023
- Dalpe, C., Baker, D.R. 2000. Experimental investigation of large-ion-lithophile-element, high-field-strength-element, and rare-earth-element partitioning between calcic amphibole and basaltic melt: the effects of pressure and oxygen fugacity. *Contributions to Mineralogy and Petrology 140*, 233–250.
- Debon, F., Le Fort, P. 1983. A chemical-mineralogical classification of common plutonic rocks and associations. *Transactions of the Royal Society of Edinburgh: Earth Sciences* 73, 135–149. DOI: 10.1017/S0263593300010117
- Deer, W. A., Howie, R. A., Zussman, J. 2013. An Introduction to the Rock-Forming Minerals. *Mineralogical Society of Great Britain and Ireland*. https://doi.org/10.1180/DHZ (cited in Supplementary Material 5).
- Eby, N.G. 1992. Chemical subdivision of the A-type granitoids: petrogenetic and tectonic implications. *Geology* 20, 641–644.
- Feng, Y., Pan, Y., Xiao, B., Chu, G., Chen, H. 2023. Hydrothermal alteration of magmatic titanite: Implications for REE remobilization and the formation of ion-adsorption HREE deposits, South China. *American Mineralogist 108*, 2051–2064. DOI: 10.2138/am-2022-8644
- Freise, M., Holtz, F., Nowak, M., Scoates, J., Strauss, H. 2009. Differentiation and crystallization conditions of basalts from the Kerguelen large igneous province: An experimental study. *Contributions to Mineralogy and Petrology 158*, 505–527. DOI: 10.1007/s00410-009-0394-5
- Frost, C.D., Frost, B.R. 2011. On Ferroan (A-Type) Granitoids: Their Compositional Variability and Mode of Origin. *Journal of Petrology* 52(1), 39–53. DOI:10.1093/petrology/egq070
- Förster, H.J. 2000. Cerite-(Ce) and thorian synchysite-(Ce) from the Niederbobritzsch granite, Erzgebirge, Germany: Implications for the differential mobility of the LREE and Th during alteration. *The Canadian Mineralogist* 38, 67–79. DOI: 10.2113/gscanmin.38.1.67
- GabbroSoft 2020. Mineral formula calculation spreadsheets. Available at: http://www.gabbrosoft.org (accessed October 2025). (cited in Supplementary Material 4).
- Gmochowska, W., Harlov, D.E., Słaby, E., Jokubauskas, P., Słáma, J., Łącki, M. 2024a. Experimental metasomatic alteration of titanite in a series of metamorphic fluids at 700 °C and 200 MPa. *Mineralogy and Petrology 118*, 321–344. DOI:10.1007/s00710-024-00862-5
- Gmochowska, W., Wirth, R., Słaby. E., Anczkiewicz, R., Krzątała, A., Roddatis, V., Sláma, J., Kozub-Budzyń, G.,

- Bhattacharya, S., Schreiber, A. 2024b. Hydrothermal alteration of accessory minerals (allanite and titanite) in the late Archean Closepet granitoid (Dharwar Craton, India): A TEM study. *Geochemistry* 84,126–130. DOI: 10.1016/j.chemer.2024.126130
- Henry, D.J., Guidotti, C.V., Thomson, J.A. 2005. The Ti-saturation surface for low-to-medium pressure metapelitic biotites: Implications for geothermometry and Ti-substitution mechanisms. *American Mineralo*gist 90, 316–328. DOI: 10.2138/am.2005.1498
- Irving, A.J., Green, D.H. 2008. Phase Relationships of Hydrous Alkalic Magmas at High Pressures: Production of Nepheline Hawaiitic to Mugearitic Liquids by Amphibole-Dominated Fractional Crystallization Within the Lithospheric. *Journal of Petrology* 49(4), 741–756. https://doi.org/10.1093/petrology/egm088
- Kontonikas-Charos, A., Ciobanu, C.L., Cook, N.J. 2014. Albitization and redistribution of REE and Y in IOCG systems: Insights from Moonta-Wallaroo, Yorke Peninsula, South Australia. *Lithos* 208–209, 178–201. https://doi.org/10.1016/j.lithos.2014.09.001
- Kowallis, B., Christiansen, E., Dorais, M., Winkel, A., Henze, P., Franzen, L., Mosher, H. 2022. Variation of Fe, Al, and F Substitution in Titanite (Sphene). *Geosciences* 12, 229. DOI: 10.3390/geosciences12060229
- Leake, B.E., Woolley, A.R., Arps, C.E.S., Birch, W.D., Gilbert, M.C., Grice, J.D., Hawthorne, F.C., Kato, A., Kisch, J.H., Krivovichev, G., Linthout, K., Laird, J., Mandarino, J.A., Maresch, W.V., Nickel, E.H., Rock, N.M.S., Schumacher, J.C., Smith, D.C., Stephenson, N.C.N., Ungaretti, L., Whittaker, E.R.J., Youzhi, G. 1997. Nomenclature of amphiboles: Report of the Subcommittee on Amphiboles of the International Mineralogical Association, Commission on New Minerals and Mineral Names. *The Canadian Mineralogist* 35, 219–246.
- Li, X., Zhang, C., Behren, H., Holtz, F. 2020. Calculating biotite formula from electron microprobe analysis data using a machine learning method based on principal components regression. *Lithos 35*. DOI: 10.1016/j. lithos.2020.105371 (cited in Supplementary Material 3).
- Liu, Y., Yang, Z., Brzozowski, M., Hao, H., Sun, J., Zhang, Y. 2025. Magma fO₂ and Volatiles in the Sub-Economic Ermi Porphyry Cu System in Northeastern China: Implications for Porphyry Cu Fertility. *Journal* of Petrology 66(5). DOI: 10.1093/petrology/egaf038
- Marshall, D. 1996. Ternplot: An Excel spreadsheet for Ternary diagrams. *Computers and Geosciences 22(6)*, 697–699. DOI:10.1016/0098-3004(96)00012-x
- Middleton, A.W., Förster, H.-J., Uysal, I.T., Golding, S.D., Rhede, D. 2012. Accessory phases from the Soultz monzogranite, Soultz-sous-Forets, France: Implications for titanite destabilization and differential REE, Y and Thmobility in hydrothermal systems. *Chemical Geology* 335, 105–117. DOI: 10.1016/j.chemgeo.2012.10.047
- Morad, S., El-Ghali, M., Caja, M., Al-Ramadan, K., Mansurbeg, H. 2009. Hydrothermal alteration of magmatic

- titanite: Evidence from Proterozoic granitic rocks, Southeastern Sweden. *The Canadian Mineralogist* 47(4), 801–811. DOI: 10.3749/canmin.47.4.801
- Munoz, J.L. 1984. F-OH and Cl-OH exchange in micas with applications to hydrothermal ore deposits. *Geochimica et Cosmochimica Acta 48*, 359–366. (cited in Supplementary Material 3).
- Munoz, J.L. 1992. Calculation of HF and HCl fugacities from biotite compositions: Revised equations. *Geological Society of America Abstracts with Programs 24*, 231. (cited in Supplementary Material 3).
- Nachit, H., Ibhi, A., Abia, E., Ben Ohoud, M. 2005. Discrimination between primary magmatic biotites, reequilibrated biotites and neoformed biotites. *C.R. Geoscience 337*, 1415–1420. DOI: 10.1016/j. crte.2005.09.002
- Pearce, J.A., Harris, N.B., W., Tindle, A.G. 1984. Trace element discrimination diagrams for the tectonic interpretation of granitic rocks. *Journal of Petrology 25(4)*, 956–983.
- Sababa, E., Gentry, F., Ndjigui, P., Onana, P., Seyoa, D. 2021. Petrography and geochemistry of sulfurous volcanic scoria from Mount Cameroon area, Central Africa: Implications for Au-PGE exploration. *Journal of African Earth Sciences 176 (2021)*, 104–144. DOI: 10.1016/j.jafrearsci.2021.104144
- Shelley, D. 1993. *Igneous and Metamorphic Rocks under the Microscope: Classification, textures, microstructures and mineral preferred orientations.* London: Chapman & Hall, 445 pp.
- Skridlaite, G., Wiszniewska, J., Duchesne, J.-C. 2003. Ferro-potassic A-type granites and related rocks in NE Poland and S Lithuania: west of the East European Craton. *Precambrian Research 124 (2003)*, 305–326. DOI: 10.1016/S0301-9268(03)00090-1
- Skridlaitė, G., Baginski, B., Whitehouse, M. 2008. Significance of ~ 1.5 Ga zircon and monazite ages from charnockites in southern Lithuania and NE Poland. *Gondwana Research 14*, 662–674. DOI:10.1016/j. gr.2008.01.009
- Skridlaitė, G., Šiliauskas, L., Prušinskienė, S., Bagiński, B. 2019. Petrography and mineral chemistry of the Varena iron ore deposit, southeastern Lithuania: Implications for the evolution of carbonate and silicate rocks and ore mineralization. *Baltica 32*, 107–126. https://doi.org/10.5200/baltica.2019.1.9
- Skridlaite, G., Siliauskas, L., Whitehouse, M.J., Johansson, Å., Rimsa, A. 2021. On the origin and evolution of the 1.86–1.76 Ga Mid-Baltic Belt in the western East European Craton. *Precambrian Research 367*, 106–403. DOI:10.1016/j.precamres.2021.106403
- Skridlaite, G., Siliauskas, L., Söderlund, U., Næraa, T. 2024. Iron-rich Ca-Mg skarns from the SW East European Craton (Lithuania): Microstructural study, mineral reactions and direct age constraints of ore-forming events using LA-ICPMS. *LITHOS* 482–483(2024), 107–736 DOI: 10.1016/j.lithos.2024.107736
- Stein, H.J., Sundblad, K., Markey, R.J., Morgan, Motu-

- za, G. 1998. Re-Os ages for Archean molybdenite and pyrite, Kuittila-Kivisuo, Finland and Proterozoic molybdenite, Kabeliai, Lithuania: Testing the chronometer in a metamorphic and metasomatic setting. *Mineralium Deposita* 33, 329–345. DOI:10.1007/s001260050153
- Sundblad, K., Mansfeld, J., Motuza, G., Ahl, M., Claesson, S. 1994. Geology, Geochemistry and Age of a Cu-Mo-Bearing Granite at Kabeliai, Southern Lithuania. *Mineralogy and Petrology* 50, 43–57. DOI: 10.1007/BF01160138
- Tindle, A.G., Webb, P.C. 1990. Estimation of lithium contents in trioctahedral micas using microprobe data. *European Journal of Mineralogy* 2, 595–610. (cited in Supplementary Material 3).
- Vandenberghe, R., De Resende, V., Da Costa, G., De Grave, E. 2010. Study of loss-on-ignition anomalies found in ashes from combustion of iron-rich coal. *Fuel* 89, 2405–2410. DOI: 10.1016/j.fuel.2010.01.022
- Vejelyte, I., Bogdanova, S., Skridlaite, G. 2015. Mesoproterozoic AMCG suites in Lithuania: petrological and

- geochronological constraints. *Estonian Journal of Earth Sciences 64(3)*, 189–198. DOI: 10.3176/earth.2015.26
- Vernon, R.H. 2004. *A Practical Guide to Rock Microstructure*. Cambridge University Press. DOI: 10.1017/CBO9780511807206
- Whitney, D.L., Evans, B.W. 2010. Abbreviations for names of rock-forming minerals. *American Mineralogist* 95, 185–187. DOI: 10.2138/am.2010.3371
- Wiszniewska, J., Claesson, S., Stein, H., Vander Auwera, J., Duchesne, J.-C. 2002. The north-eastern Polish anorthosite massifs: petrological, geochemical and isotopic evidence for a crustal derivation. *Terra Nova* 14, 451–460.
- Xiao, X., Zhou, T., White, N.C., Zhang, L., Fan, Y., Chen, X. 2020. Multiple generations of titanites and their geochemical characteristics record the magmatic hydrothermal processes and timing of the Dongguashan porphyry-skarn Cu-Au system, Tongling district, Eastern China. *Mineral Deposit* 56, 363–380. DOI: 10.1007/s00126-020-00962-0

Supplementary Material Online